



### **Science Arts & Métiers (SAM)**

is an open access repository that collects the work of Arts et Métiers Institute of Technology researchers and makes it freely available over the web where possible.

This is an author-deposited version published in: <https://sam.ensam.eu>  
Handle ID: <http://hdl.handle.net/10985/17261>

#### **To cite this version :**

Mohamed Lamine ASKOURA, Fabrice VAUDELLE, Jean-Pierre L'HUILLIER - Numerical Study of Light Transport in Apple Models Based on Monte Carlo Simulations - Photonics - Vol. 3, n°1, p.2 - 2015

Any correspondence concerning this service should be sent to the repository

Administrator : [scienceouverte@ensam.eu](mailto:scienceouverte@ensam.eu)



# Numerical Study of Light Transport in Apple Models Based on Monte Carlo Simulations

Mohamed Lamine Askoura <sup>1,2,\*</sup>, Fabrice Vaudelle <sup>1</sup> and Jean-Pierre L'Huillier <sup>1</sup>

<sup>1</sup> Laboratoire Arts et Métiers ParisTech Angers (LAMPA), PRES LUNAM, École Nationale Supérieure des Arts et Métiers (ENSAM), 2 Boulevard du Ronceray, BP 93525, 49035 Angers Cedex 01, France; f.vaudelle@libertysurf.fr (F.V.); Jean-Pierre.Lhuillier@ensam.eu (J.-P.L.)

<sup>2</sup> LUNAM Université, SFR 4207 QUASAV, Groupe École Supérieure D'agriculture (ESA), UPSP Groupe de Recherche Agro-Alimentaire sur le Produit et Procédés (GRAPPE), 55 Rue Rabelais, BP 30748, 49007 Angers Cedex 01, France

\* Correspondence: ml.askoura@gmail.com; Tel.: +33(0)-241-207-373; Fax: +33(0)-241-207-350

**Abstract:** This paper reports on the quantification of light transport in apple models using Monte Carlo simulations. To this end, apple was modeled as a two-layer spherical model including skin and flesh bulk tissues. The optical properties of both tissue types used to generate Monte Carlo data were collected from the literature, and selected to cover a range of values related to three apple varieties. Two different imaging-tissue setups were simulated in order to show the role of the skin on steady-state backscattering images, spatially-resolved reflectance profiles, and assessment of flesh optical properties using an inverse nonlinear least squares fitting algorithm. Simulation results suggest that apple skin cannot be ignored when a Visible/Near-Infrared (Vis/NIR) steady-state imaging setup is used for investigating quality attributes of apples. They also help to improve optical inspection techniques in the horticultural products.

**Keywords:** apple models; light transport; skin; flesh; computed backscattering images; assessment of optical properties

---

## 1. Introduction

Propagation of light in turbid tissues such as biological tissues, fruits and vegetables is a complex mechanism which involves scattering and absorption. Incident photons that penetrate in turbid tissues often undergo multiple scattering events before being absorbed or exiting from the material. Light absorption is primarily due to chemical constituents (chromophores and pigments) of the material [1–3], whereas light scattering is more related to structural features (density, particle size, and cellular structures) [4–6]. These two fundamental optical events are characterized by the absorption coefficient  $\mu_a$ , the scattering coefficient  $\mu_s$ , the scattering anisotropy  $g$ , the reduced scattering coefficient  $\mu'_s$  ( $\mu'_s = \mu_s(1 - g)$ ), and the refractive index ( $n$ ) [7,8]. Knowledge of these macroscopic optical coefficients is required to gain insight into light tissue interaction process, or to improve the optimization of the non-invasive (non-destructive) diagnostics technologies. Various optical methods have been developed to quantify light absorption and scattering in biological samples. They have been previously reported for non-invasive assessment of the optical properties of biological tissues and may be classified as spatially-resolved, time-resolved, and frequency-resolved methods [9,10]. All these methods allow us to extract the optical properties of turbid tissues, provided that an appropriate radiation transfer equation coupled with an inverse algorithm is used to fit the reflectance data [11–13]. Optical techniques devoted to the measurements of quality attributes of fruits, and food products mainly concern the hyperspectral imaging-based spatially-resolved method [14–17], and time-resolved method [1,2,18,19]. Studies carried out by means of these two systems were based on the major

assumption that the interrogated samples are plane and homogeneous. These assumptions may not be well appropriate because most fruits are at least composed of two layers of tissues, *i.e.*, skin and flesh, and also present a local curvature (or size) that cannot be assimilated to a plan boundary. Therefore, it seems more realistic to develop a two-layer or multi-layer model with curved boundary to study light propagation in whole fruit, and quantify the effect of the surrounding layer (skin) on the assessment of the flesh optical properties [20]. Several studies have provided analytical solutions to diffusion problem for layered media [21–23]. These models can be applied only in relatively simple configurations such as slabs with different homogeneous layers for which the light scattering prevails over the absorption ( $\mu'_s \gg \mu_a$ ). Because the diffusion approximation is inaccurate near the boundary, application of these models requires that the thickness of the first layer be larger than its reduced transport mean free path ( $1/\mu_a + \mu'_s$ ). Other works have described numerical methods based on finite element [24–26] and Monte Carlo (MC) [6,27–34] models to simulate light transport in various complex multilayered biological structures. The Monte Carlo method has also been successfully used in the context of food and agricultural products for predicting optical features related to apples [20,35], kiwi fruit [36], and onion bulbs [37]. Although the MC method requires the propagation of substantial numbers of photons and large amounts of computing time to obtain statistically reliable results, it can solve the radiative transfer equation [38] without the limitations of complex sample geometries and optical properties.

This research was aimed at the development of a Monte Carlo model to simulate and quantify light propagation in apple tissue structures. The ultimate goal was to reveal the role played by the skin layer on the light transport features including backscattering images, steady-state diffuse reflectance profiles, internal sensibility profiles of photons, and penetration depth in the flesh. This paper is outlined as follows. In Section 2, we describe the Monte Carlo algorithm, apple tissue model based on a two-layer spherical geometry (skin and flesh), as well as two imaging-tissue setups related to whole and half-cut apples, with and without skin. In Section 3, we perform various simulations with a careful consideration of tissue optics and metrics. Simulation results are detailed with further information on the optimum sensing range which provides at the best the retrieved flesh optical properties in the case of an imaged whole apple. Finally, we conclude with prospects in Section 4.

## 2. Methodology

### 2.1. Monte Carlo Algorithm

Monte Carlo method allows us to simulate radiation transport in turbid media according to probabilities of mean free path  $l_p$ , direction change due to scattering, absorption and Fresnel reflection [27]. These probabilities depend on the optical parameters  $\mu_s$ ,  $\mu_a$ ,  $g$  and  $n$ , which are assigned to the tissues. Here we used a Monte Carlo code described in a previous paper [20] that was adapted to both imaging setups displayed in Figure 1a,b.

Each tissue model is illuminated by a Gaussian collimated beam ( $\omega_0 = 0.5$  mm at  $1/e^2$ ) assumed in normal incidence. This is an acceptable approach to the problem (Figure 1a) if the angle between the source axis and detector axis is not too large ( $<10^\circ$ ). Preliminary apple experiments carried out by means of a homemade multispectral imaging system [39] have confirmed that the backscattering reflectance profiles have few distortions (symmetry) for incidence angles less than  $10^\circ$ . Moreover, in practical fruit diagnostics [39,40] the numerical aperture of the camera contributes to confine an effective area over the sample surface ( $\sim 25$  mm). In this paper, the Monte Carlo simulations take into account all backscattered photons coming out from a limited area of diameter 20 mm, at the considered surface of the fruit. The main steps of the Monte Carlo algorithm are depicted in the flowchart (Figure 2), and are summarized below:

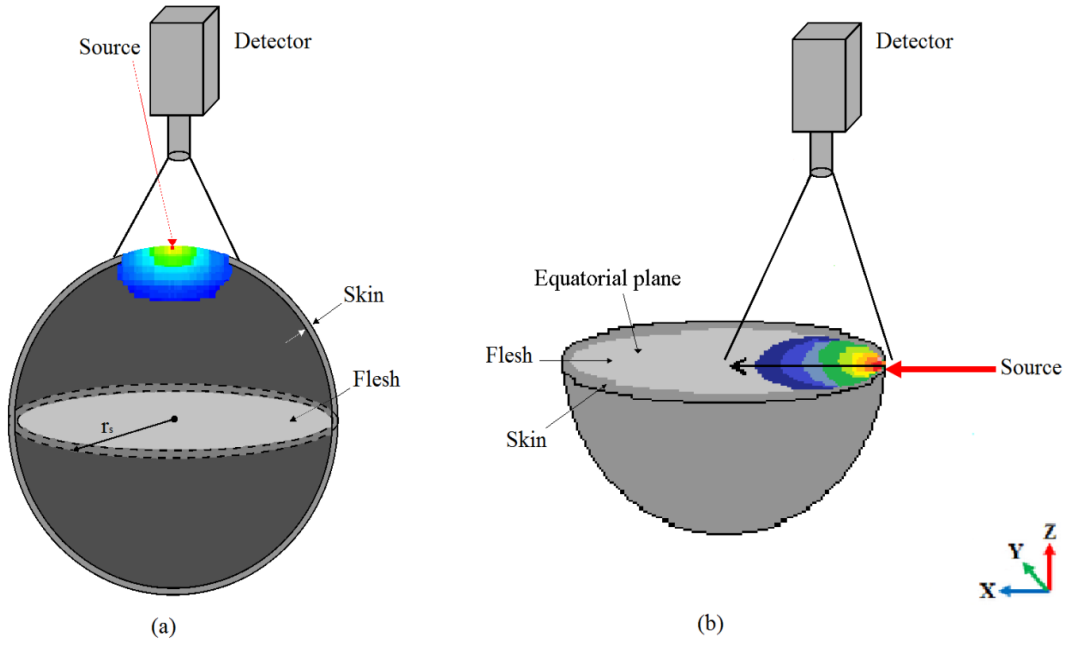


**Figure 1.** Apple models and imaging-tissue setups used for the Monte Carlo simulations. (a) Whole apple assimilated to a sphere (flesh) surrounded by a thin layer of tissue (skin), and observed over its top curved boundary; (b) Half-cut spherical apple model observed over its equatorial plane. In both cases, the Gaussian beam size of the incident light source is  $2\omega_0 = 1$  mm.

- The emission point of a photon in the Gaussian beam is randomly determined to generate the coordinates  $x_0, y_0$ . Given  $\varepsilon_1$  and  $\varepsilon_2$  independently uniformly distributed in  $[-1,1]$ , set  $R = (2\varepsilon_1 - 1)^2 + (2\varepsilon_2 - 1)^2 < 1$ , and  $z_0$  is close to the local curvature of the model. Then the coordinates  $x_0$  and  $y_0$  are computed as [41]

$$x_0 = \frac{w_0}{2} (2\varepsilon_1 - 1) \sqrt{\frac{-2\ln R}{R}} \quad (1)$$

$$y_0 = \frac{w_0}{2} (2\varepsilon_2 - 1) \sqrt{\frac{-2\ln R}{R}} \quad (2)$$

- To simulate propagation, Monte Carlo method requires defining a distance for the collision (step size). The step size of the photon is computed based on the sampling of the probability distribution for mean free path  $l_P = \frac{1}{\mu_t} (\mu_t = \mu_a + \mu_s)$ .

$$S = \frac{-\ln \varepsilon_3}{\mu_t} \quad (3)$$

$S \in [0, \infty]$ , where  $\varepsilon_3$  is a random number uniformly distributed over  $[0,1]$ .

- Once the photon has taken a step, some of the photon weight  $W_k$  (initial value  $W_0 = 1$ ) decrease due to absorption by tissue sample must occur. Therefore,

$$W_k = \left[ 1 - \frac{\mu_a}{\mu_t} \right] W_{k-1} \quad (4)$$

until weight falls below a threshold value  $W_{th}$  (associated to a Russian roulette technique).

- Once the photon has been moved and its weight decremented, the photon is ready to be scattered. A random number  $\varepsilon_4$  is generated, and the selection of the deflection angle  $\theta$ , is accomplished using the probability density function  $P_{HG}(\cos \theta)$  of scattering in tissue (Henyey-Greenstein) [42]

$$P_1 = \frac{1}{2g} \left[ 1 + g^2 - \left( \frac{1 - g^2}{1 - g + 2g\varepsilon_4} \right)^2 \right]; g > 0 \quad (5)$$

where  $\theta = \cos^{-1}(P_1)$ , and  $\varphi = 2\pi\varepsilon_5$ : uniformly distributed within the interval  $[0, 2\pi]$ . Once the deflection  $\theta$  and azimuthal  $\varphi$  angles are chosen, the new direction for the photon propagation  $(K'_x, K'_y, K'_z)$  is computed from the three direction cosines  $(K_x, K_y, K_z)$  using the formulas [43,44]

$$K'_x = \frac{\sin(\theta)}{\sqrt{1 - K_z^2}} (K_x K_z \cos(\varphi) - K_y \sin(\varphi)) + K_x \cos(\theta) \quad (6)$$

$$K'_y = \frac{\sin(\theta)}{\sqrt{1 - K_z^2}} (K_y K_z \cos(\varphi) - K_x \sin(\varphi)) + K_y \cos(\theta) \quad (7)$$

$$K'_z = -\sin(\theta) \cos(\varphi) \sqrt{1 - K_z^2} + K_z \cos(\theta) \quad (8)$$

To avoid division by zero, if the angle is too close to normal (i.e.,  $|K_z| \sim 1$ ), the following formulas are used [40], instead of Equations (6)–(8).

$$K'_x = \sin(\theta) \cos(\varphi) \quad (9)$$

$$K'_y = \sin(\theta) \sin(\varphi) \quad (10)$$

$$K'_z = \text{sign}(K_z) \cos(\theta) \quad (11)$$

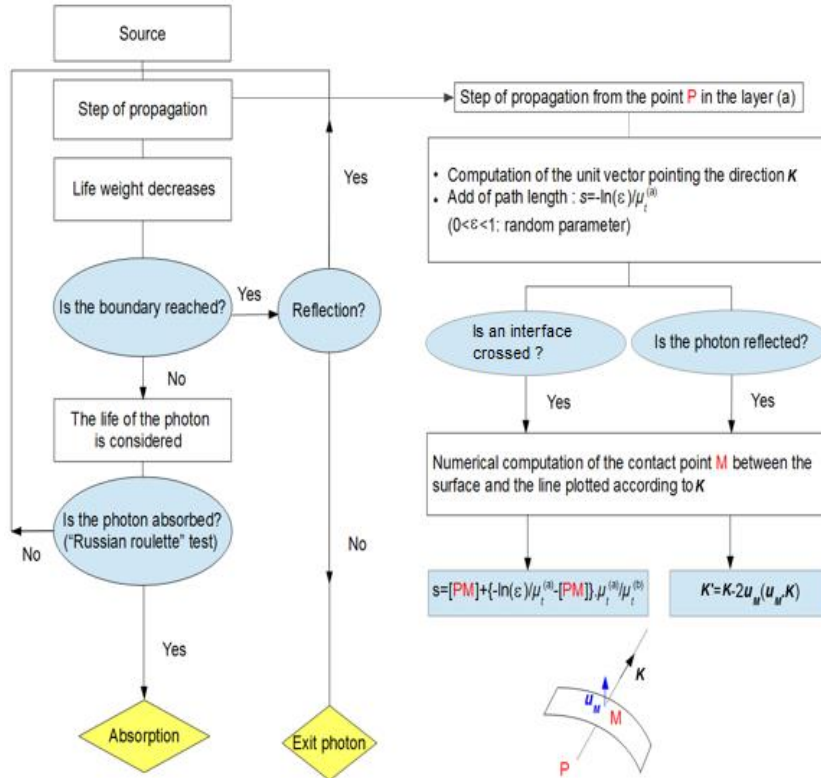


**Figure 2.** Flowchart of the fundamental steps of the Monte Carlo simulations.

- During a step, a photon may attempt to escape the spherical apple model (with and without skin layer) at the air–tissue interface. Then, the photon may either escape and contributes to the observed reflectance or be internally reflected by the interface (flesh or skin). Snell's law, which gives the relationship between the angle of incidence  $\theta_i$  and the angle of transmittance  $\theta_t$  (and refractive indexes), allows us to calculate the internal reflectance  $R(\theta_i)$ , according to the Fresnel's law

$$n_i \sin(\theta_i) = n_t \sin(\theta_t) \quad (12)$$

$$R(\theta_i) = \frac{1}{2} \left[ \frac{\sin^2(\theta_i - \theta_t)}{\sin^2(\theta_i + \theta_t)} + \frac{\tan^2(\theta_i - \theta_t)}{\tan^2(\theta_i + \theta_t)} \right] \quad (13)$$

If  $R(\theta_i) < \varepsilon_6$ , then the photon escapes the boundary (skin–air) and account for the backscattering data.

If  $R(\theta_i) > \varepsilon_6$ , then the photon is internally reflected and its direction cosine is updated by reversing the change of direction.

A great task was also to determine the interaction point between the photon path and the sphere boundary. A procedure based on an optimization scheme was used to estimate the incidence point close to the considered boundary (flesh–air, flesh–skin and/or skin–air). For a photon coming from a point P ( $x_P, y_P, z_P$ ) and crossing at the point M ( $x_M, y_M, z_M$ ), the coordinate  $z_M$  may be found by solving the set of two equations:

$$z_M = \pm \sqrt{r_b^2 - (x_P + \gamma \cdot K_x)^2 - (y_P + \gamma \cdot K_y)^2} = h_1(\gamma) \quad (14)$$

$$z_M = z_P + \gamma \cdot K_z = h_2(\gamma) \quad (15)$$

where  $r_b$  is the radius of the spherical boundary, and  $\gamma$  the length from P to M. An iterative scheme is then used to minimize the difference  $|h_1(\gamma) - h_2(\gamma)|$ , yielding the optimal value  $\gamma = \gamma_{opt}$ . Finally, the coordinates of the point M are given by ( $x_P + \gamma_{opt} \cdot K_x, y_P + \gamma_{opt} \cdot K_y, z_P + \gamma_{opt} \cdot K_z$ ).

Another series of events arise when the photon hits an interface (skin–flesh). The new photons step size should be expressed as follows:

$$S_{new} = PM + [S - PM] \frac{\mu_t}{\mu_t^{new}} \quad (16)$$

where  $PM$  is equal to  $\gamma_{opt}$ . The Monte Carlo code was developed on the base of Matlab 8.a, and implemented on a PC (Processor Intel Core i5, 2.6 GHz).

## 2.2. Monte Carlo Input Data

In order to perform simulation, the Monte Carlo model requires defining the sample geometry parameters, and the optical properties of each considered tissue type (skin or flesh) as a part of the input data. The radius  $r_s$  of the apple models described in Figure 1a,b was set at 35 mm, in agreement with the mean value measured in our laboratory for three apple varieties (Royal Gala, Golden Delicious and Granny Smith), but also with data reported by others [40,45].

Skin features have been well documented from histological observation [46,47]. The apple peel consists of flat cells whose sizes evolve rapidly from the surface to deep depths, through distinct layer types. The subsurface tissue is mainly composed of cuticle, epidermis, and hypodermis. Skin thickness values reported in the literature range from 50  $\mu\text{m}$  to 100  $\mu\text{m}$ , since hypodermis layers are ignored.

Measurements carried out with a confocal microscope have confirmed these data with a mean skin thickness value of 80  $\mu\text{m}$  (Table 1). To this end, small slices of the three apples were removed with a surgical blade. Cut-samples were viewed at 100 $\times$  enlargement using a Nikon A1S1 confocal laser scanning microscope interfaced to a digital camera, and the captured images were analyzed with ImageJ software. The skin thickness was estimated from the boundary where a fast growth of the cells

was noted. Different values of the reduced scattering and absorption coefficients related to the flesh ( $\mu_a^{(f)}$ ,  $\mu_s'^{(f)}$ ), and the skin ( $\mu_a^{(s)}$ ,  $\mu_s'^{(s)}$ ) of three apple setup (Royal Gala, Golden Delicious and Granny Smith) are listed in Table 2. The data concerning the flesh have been reported by authors who worked with the hyperspectral imaging-based spatially-resolved method [48,49] or with the time-resolved method [1,2], in the wavelengths ranging from 633 nm to 850 nm.

The listed data especially show the variation between retrieved optical properties due to considered apple varieties or to the optical technique which has been used for the measurements. It should also be noted that the absorption and reduced scattering coefficients of the skin are both higher than those of the flesh tissue [50]. Finally, for all simulations, the anisotropy factor ( $g$ ) was set at 0.8 [8,37], whereas the refractive indexes  $n = 1.4$  and  $n = 1$  were, respectively, used for the apple turbid models and the outside. In order to obtain reliable computational results, the number of launched photons was varied from  $0.5 \times 10^6$  to  $2 \times 10^6$  with respect to each investigated imaging tissue setup.

**Table 1.** Apple skin thickness measured with a confocal microscope.

Apples	Skin Thickness ( $\mu\text{m}$ )
Royal Gala	$65.6 \pm 13.3$
Granny Smith	$91.3 \pm 13.8$
Golden Delicious	$78.1 \pm 09.1$

**Table 2.** Optical properties of studied apple varieties ( $\text{mm}^{-1}$ ).

Apples	Wavelengths	Flesh $\mu_a^{(f)}$	Flesh $\mu_s'^{(f)}$	Skin $\mu_a^{(s)}$	Skin $\mu_s'^{(s)}$
Gala	750–850 nm	$\sim 0.1 \pm 0.1^{(1)}$	$\sim 1.2^{(1)}$	$\sim 0.15 \pm 0.1^{(1)}$	$3.75^{(1)}$
		$\sim 0.0125^{(2)}$	$1.15 \pm 0.3^{(2)}$		
		$\sim 0.1 \pm 0.1^{(1)}$	$\sim 1.2^{(1)}$		
Granny	750–850 nm	$\sim 0.04 \pm 0.03^{(1)}$	$\sim 1.2^{(1)}$	$\sim 0.075 \pm 0.03^{(1)}$	$4.25^{(1)}$
		$\sim 0.004^{(4)}$	$\sim 2^{(4)}$		
		$\sim 0.1 \pm 0.1^{(1)}$	$\sim 1.2^{(1)}$		
Golden	750–850 nm	$0.005 \pm 0.0025^{(5)}$	$1.1 \pm 0.1^{(5)}$	$\sim 0.5 \pm 0.1^{(1)}$	$\sim 4^{(1)}$
		$\sim 0.01^{(3)}$	$0.8 \pm 0.1^{(3)}$		
		$\sim 0.004^{(4)}$	$\sim 2^{(4)}$		
	633 nm	$\sim 0.04^{(3)}$	$0.85 \pm 0.15^{(3)}$		
		$0.004 \pm 0.0025^{(5)}$	$1.4 \pm 0.15^{(5)}$		

(1) Saeys *et al.*, 2008 [50]; (2) Rowe *et al.*, 2014 [48]; (3) Lu *et al.*, 2010 [49]; (4) Cubeddu *et al.*, 2001 [1]; (5) Cubeddu *et al.*, 2001 [2].

### 3. Results and Discussion

#### 3.1. Imaging Whole Apple

To show the effect of the skin on light diffusion process in whole apple illuminated with a Gaussian spot laser, backscattering images associated with their diffuse reflectance profiles were first simulated. A first series of results was carried out by considering the whole apple as unpeeled or peeled. Typical backscattering images are displayed in Figure 3a–c. For convenience of direct comparisons, each presented image has been normalized with respect to its peak intensity.

In the cases of Figure 3a,b, the whole apple is covered with a skin layer of thickness  $80 \mu\text{m}$ , whereas in the case of Figure 3c, the apple is considered peeled. The data were generated with  $\mu_a^{(f)} = 0.015 \text{ mm}^{-1}$ ,  $\mu_s'^{(f)} = 1.15 \text{ mm}^{-1}$ ,  $\mu_a^{(s)} = 0.05 \text{ mm}^{-1}$  (Figure 3a), or  $0.5 \text{ mm}^{-1}$  (Figure 3b), and  $\mu_s'^{(s)} = 4 \text{ mm}^{-1}$ . We note that changing the absorption coefficient of the skin ( $0.5 \text{ mm}^{-1}$  against  $0.05 \text{ mm}^{-1}$ ) does not affect the size of the computed backscattering images in Figure 3a,b. In contrast, the image related to the whole apple without skin (Figure 3c) appears larger with respect to the previous cases.



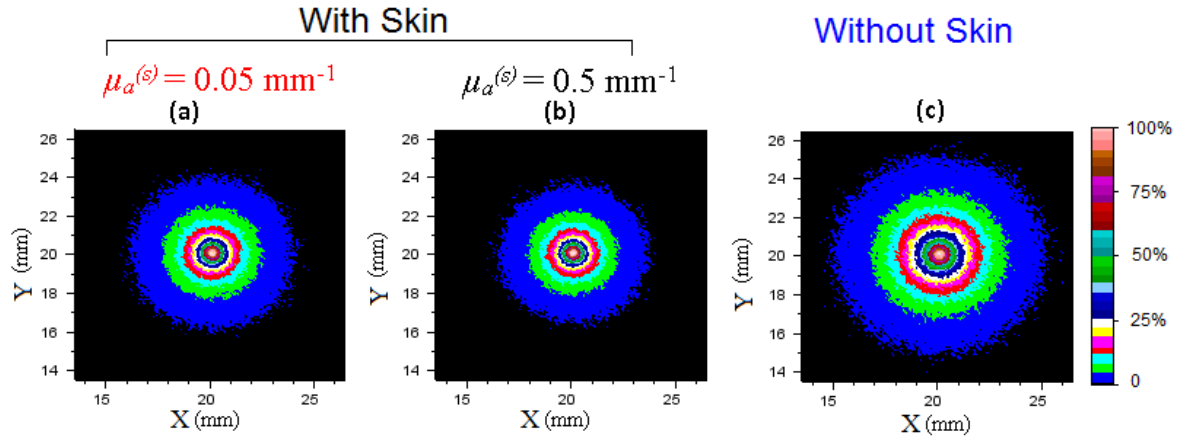


**Figure 3.** Simulated backscattering images captured at the periphery of a whole apple with skin (a), (b), and without skin (c). The images were generated with  $\mu_a^{(f)} = 0.015 \text{ mm}^{-1}$ - $\mu'_s{}^{(f)} = 1.15 \text{ mm}^{-1}$ , and (a)  $\mu_a^{(s)} = 0.05 \text{ mm}^{-1}$ - $\mu'_s{}^{(s)} = 4 \text{ mm}^{-1}$ , (b)  $\mu_a^{(s)} = 0.5 \text{ mm}^{-1}$ - $\mu'_s{}^{(s)} = 4 \text{ mm}^{-1}$ , (c)  $\mu_a^{(s)} = \mu_a^{(f)} - \mu'_s{}^{(s)} = \mu'_s{}^{(f)}$ ,  $r_s = 35 \text{ mm}$ , skin thickness of  $80 \text{ }\mu\text{m}$ , and normalized with respect to their peak intensity.

The spatial diffuse reflectance profiles corresponding to the three computed images (Figure 3), are presented in Figure 4. Overall, it is shown that the peak intensity related to an intact apple is larger than the one obtained for an apple without skin (flesh alone).

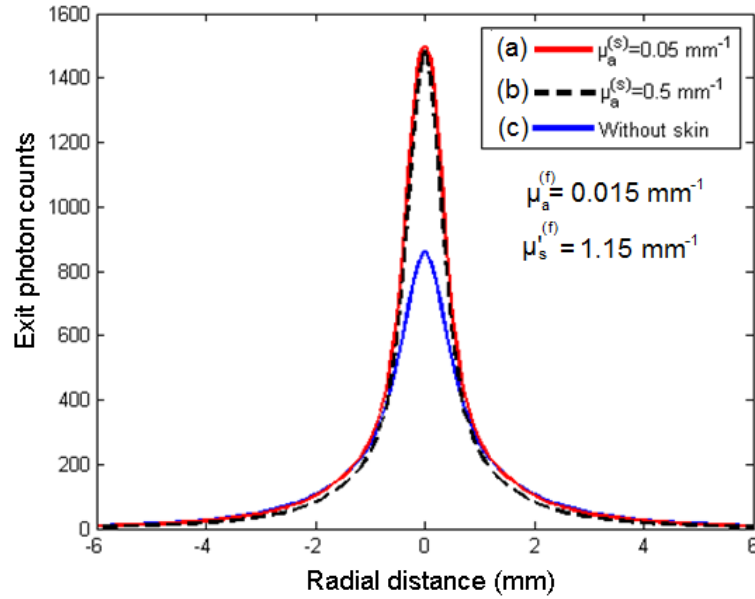


**Figure 4.** Diffuse reflectance profiles plotted as a function of the radial distance  $\rho = \sqrt{X^2 + Y^2}$ , and corresponding to the three generated images (a–c) displayed in Figure 3.

Moreover, the peak intensity is practically not affected by the absorption coefficient of the skin. According to [20], the skin acts like a screen which confines the diffused photons in the sub-surface (skin–flesh). In this case, more backscattering photons can escape the boundary (skin–air), and then contribute to increase the peak intensity of the spatial diffuse reflectance.

A second series of computation was carried out using a skin thickness fixed at  $150 \text{ }\mu\text{m}$ , while varying the optical properties  $\mu_a^{(s)}$  and  $\mu'_s{}^{(s)}$ . The resulting normalized images are displayed in Figure 5a–c, and the corresponding spatial diffuse reflectance profiles are presented in Figure 6. All the data were generated with  $\mu_a^{(f)} = 0.0075 \text{ mm}^{-1}$ - $\mu'_s{}^{(f)} = 1.25 \text{ mm}^{-1}$ , and



$\mu_a^{(s)} = 0.05 \text{ mm}^{-1}$ - $\mu_s^{(s)} = 4 \text{ mm}^{-1}$  (Figure 5a),  $\mu_a^{(s)} = 0.5 \text{ mm}^{-1}$ - $\mu_s^{(s)} = 4 \text{ mm}^{-1}$  (Figure 5b),  $\mu_a^{(s)} = 0.05 \text{ mm}^{-1}$ - $\mu_s^{(s)} = 2.5 \text{ mm}^{-1}$  (Figure 5c). At first glance, it is possible to distinguish two different trends among the generated backscattering images in Figure 5a-c. First, when the absorption coefficient  $\mu_a^{(s)}$  of the skin is increased from  $0.05 \text{ mm}^{-1}$  to  $0.5 \text{ mm}^{-1}$ , the backscattering area in Figure 5a,b shows only slight changes. Consequently, the corresponding spatial diffuse reflectance profiles (Figure 6a,b) are practically merged. Second, when the reduced scattering coefficient  $\mu_s^{(s)}$  of the skin is decreased from  $4 \text{ mm}^{-1}$  to  $2.5 \text{ mm}^{-1}$  ( $\mu_a^{(s)} = 0.05 \text{ mm}^{-1}$ ), an enlarged image size is observed. As the scattering diameter increases, the peak intensity of the corresponding reflectance profile decreases (Figure 6). This is consistent with the fact that the optical properties of the skin become closer to those of the flesh in the case of Figure 5c in comparison to the cases in Figure 5a,b.

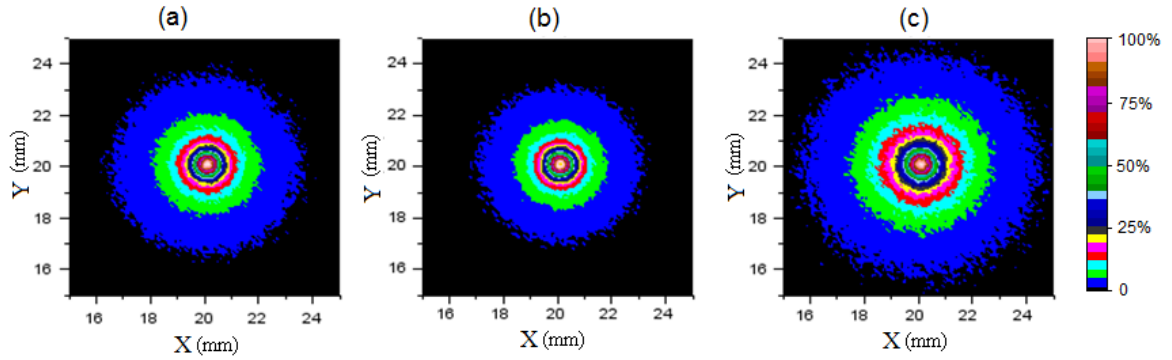


**Figure 5.** Simulated backscattering images captured over the curved boundary of a whole apple covered by a skin layer of thickness  $150 \mu\text{m}$  with different optical properties. The data were generated with  $\mu_a^{(f)} = 0.0075 \text{ mm}^{-1}$ - $\mu_s^{(f)} = 1.25 \text{ mm}^{-1}$ , (a)  $\mu_a^{(s)} = 0.05 \text{ mm}^{-1}$ - $\mu_s^{(s)} = 4 \text{ mm}^{-1}$ , (b)  $\mu_a^{(s)} = 0.5 \text{ mm}^{-1}$ - $\mu_s^{(s)} = 4 \text{ mm}^{-1}$ , (c)  $\mu_a^{(s)} = 0.05 \text{ mm}^{-1}$ - $\mu_s^{(s)} = 2.5 \text{ mm}^{-1}$ ,  $r_s = 35 \text{ mm}$ , and normalized with respect to their peak intensity.

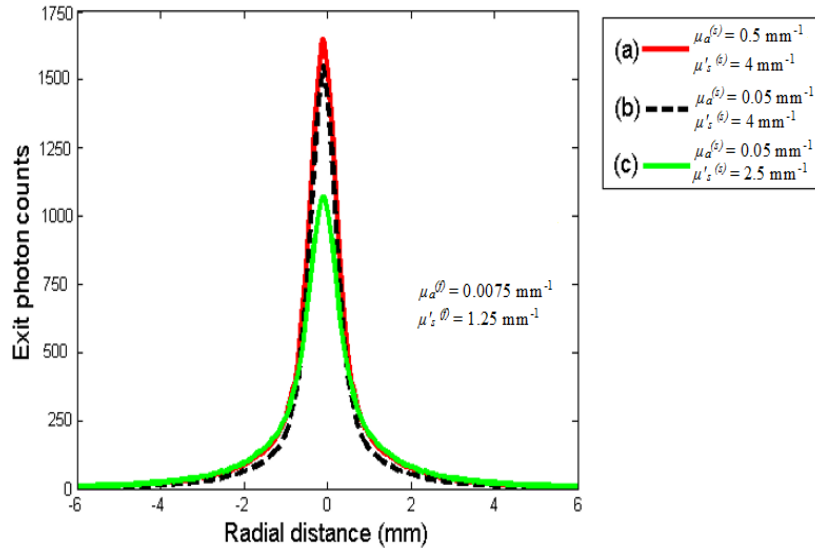


**Figure 6.** Diffuse reflectance profiles plotted as a function of the radial distance  $\rho = \sqrt{X^2 + Y^2}$ , and corresponding to the three generated images (a, c) displayed in Figure 5.

### 3.2. Imaging of Half-Cut Apple

To gain more information on the light propagation in apple structures, the model was adapted such that it mimics a half-cut apple with and without skin layer. As displayed in Figure 1b, the

light source illuminates the sample normally to the boundary, at two different locations,  $z$ , below the equatorial plane. Typical backscattering images captured by a virtual detector, facing the equatorial plane of the apple models with and without skin layer are shown in Figure 7a,c for the source located at  $z = -0.5$  mm or  $z = -3$  mm. The corresponding diffuse reflectance profiles are displayed in Figure 7b,d. All data were generated with  $\mu_a^{(f)} = 0.0075 \text{ mm}^{-1}$ ,  $\mu_s^{(f)} = 1.25 \text{ mm}^{-1}$ ,  $\mu_a^{(s)} = 0.05 \text{ mm}^{-1}$ ,  $\mu_s^{(s)} = 4 \text{ mm}^{-1}$ , and a skin thickness of  $80 \text{ }\mu\text{m}$ . In both investigated cases, the photon patterns stay close to the impact point of the light source, but the maximum density varies from each other.

When the source is near the plane surface ( $z = -0.5$  mm, Figure 7a,b), the skin has the effect to shift the isolines near the curved boundary, and the peak intensity of the diffuse reflectance profile (Figure 6b) occurs at the distance of about 0.25 mm. In contrast, the peak intensity of the diffuse reflectance profiles computed for the flesh (without skin) is less sharp but occurs at about 0.5 mm. The effect of the skin weakens when the source is located further down ( $z = -3$  mm) Figure 7c,d. A large scattering amount tends to uniformize the different events observed, while decreasing the recorded diffuse intensity. Therefore, the isolines (Figure 7c) related to unpeeled and peeled apple are barely shifted, and the corresponding diffuse reflectance profiles (Figure 7d) are practically merged. Furthermore, the peak intensity of both diffuse reflectance profiles occurs at the distance of 1.25 mm from the sample boundary.

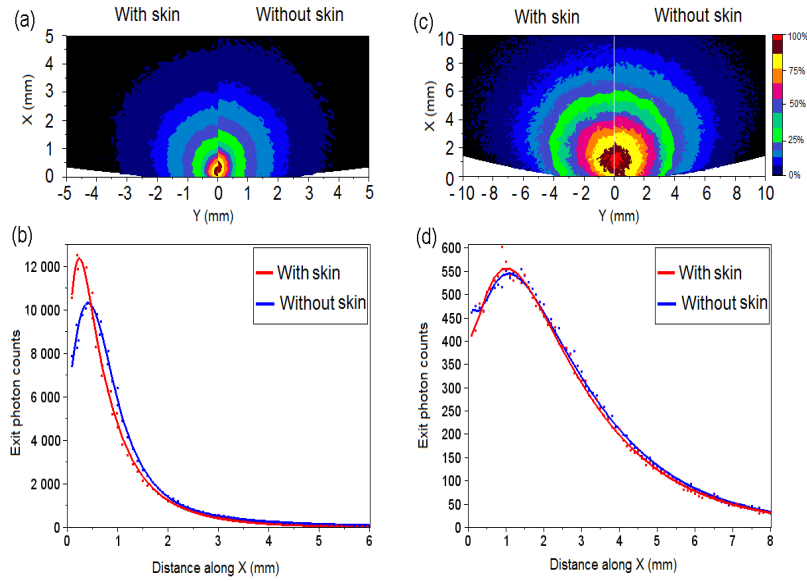


**Figure 7.** Simulated backscattering images (a)–(c) captured over the equatorial plane of half-cut apple models with and without skin, and corresponding diffuse reflectance profiles (b)–(d), plotted along  $X$  for  $Y = 0$  and  $Z = 0$ . (a)–(b) Source located at  $z = -0.5$  mm from the plane surface, and (c)–(d) source located at  $z = -3$  mm. The data were generated with  $\mu_a^{(f)} = 0.0075 \text{ mm}^{-1}$ ,  $\mu_s^{(f)} = 1.25 \text{ mm}^{-1}$ ,  $\mu_a^{(s)} = 0.05 \text{ mm}^{-1}$ ,  $\mu_s^{(s)} = 4 \text{ mm}^{-1}$ ,  $r_s = 35$  mm, and skin thickness of  $80 \text{ }\mu\text{m}$ .

In both cases, backscattered light increases the incident light source, yielding an internal fluence rate that exceeds the irradiance delivered at the apple surface. This is in agreement with numerical findings of others, who showed that the peak and depth position of the fluence rate depend on the illuminating beam radius [26,51].

### 3.3. Assessment of Internal Optical Properties

In this subsection, we assess the optical properties of the apple flesh. The method is based on a diffusion theory model to fit the diffuse reflectance profiles and then to extract the unknown

coefficients  $\mu_a$  and  $\mu'_s$ . The analytical model of Kienle and Patterson [52] was chosen for these investigations. The diffuse reflectance  $R_d(\rho)$  generated at the radial distance  $\rho$ , from a point source acting at  $z_0 = 1/\mu'_t$  ( $\mu'_t = \mu_a + \mu'_s$ ) in a homogeneous semi-infinite diffusing medium is as follow:

$$R_d(\rho) = C_1 \Phi(\rho, z = 0) + C_2 R_{flux}(\rho) \quad (17)$$

$$\Phi(\rho, z = 0) = \frac{1}{4\pi D} \left[ \frac{e^{(-\mu_{eff} r_1)}}{r_1} - \frac{e^{(-\mu_{eff} r_2)}}{r_2} \right] \quad (18)$$

$$R_{flux}(\rho) = \frac{1}{4\pi} \left[ z_0 \left( \mu_{eff} + \frac{1}{r_1} \right) \frac{e^{(-\mu_{eff} r_1)}}{r_1^2} + (z_0 + 2z_b) \left( \mu_{eff} + \frac{1}{r_2} \right) \frac{e^{(-\mu_{eff} r_2)}}{r_2^2} \right] \quad (19)$$

and  $\mu_{eff} = \sqrt{3\mu_a(\mu_a + \mu'_s)}$  is the effective attenuation coefficient,  $r_1 = \sqrt{z_0^2 + \rho^2}$ ,  $r_2 = \sqrt{(z_0 + 2z_b)^2 + \rho^2}$ ,  $z_b = 2AD$ ,  $D = \frac{1}{3\mu'_t}$ , ( $A = 2.945$ , for  $n = 1.4$ ) [53]. The constants  $C_1 = \frac{1}{4\pi} \int_{2\pi} [1 - R(\theta_i)] \cos\theta_i d\Omega$  and  $C_2 = \frac{3}{4\pi} \int_{2\pi} [1 - R(\theta_i)] \cos^2\theta_i d\Omega$  are both dependent on the Fresnel reflection coefficient (Equation (13)), and the solid angle  $\Omega$ . For  $n = 1.4$ ,  $C_1 = 0.118$  and  $C_2 = 0.306$  [11]. The spatial profiles covering 2.8–10 mm [39] were used in the curve fitting procedure. This radial range is in agreement with the optimum imaging range for diffuse reflectance from the surface of “Golden Delicious” apples, which was estimated to be between the upper ( $4 \times 10^2$  lux) and lower ( $4 \times 10^{-3}$  lux) detection limits of a CCD camera setup [54]. Fitting results, based on the use of the inverse nonlinear least squares algorithm (Trust-Region) implemented on Matlab 8.a, are listed Table 3. Three thicknesses of the skin ( $d = 0, 80$ , and  $150 \mu\text{m}$ ) and different combinations of optical properties  $\mu_a^{(s)} - \mu'_s^{(s)}$ ;  $\mu_a^{(f)} - \mu'_s^{(f)}$  were used as input data in the fitting procedures.

The accuracy of the retrieved method largely depends on the interplay between the optical properties which have been chosen. In the case of apple without skin layer ( $d = 0 \mu\text{m}$ ), the fitting results are better for moderate values of  $\mu_a^{(f)} - \mu'_s^{(f)}$  ( $0.025 \text{ mm}^{-1}$ – $1.25 \text{ mm}^{-1}$ ,  $0.015 \text{ mm}^{-1}$ – $1.15 \text{ mm}^{-1}$ ) than for low values ( $0.0075 \text{ mm}^{-1}$ – $0.75 \text{ mm}^{-1}$ ) or especially for a low value of  $\mu_a^{(f)}$  ( $0.0075 \text{ mm}^{-1}$ – $1.25 \text{ mm}^{-1}$ ).

When the flesh is covered with a skin layer of thickness  $d = 80 \mu\text{m}$  or  $150 \mu\text{m}$ , the relative errors on the estimates ( $\mu_a - \mu'_s$ ) increase with respect to the absorption coefficient ( $\mu_a^{(s)}$ ) of the skin. This may be explained by the fact that a small number of photons propagating through the flesh are re-emitted when the skin is relatively absorbent.

Finally, when the optical properties of the flesh are low ( $0.0075 \text{ mm}^{-1}$ – $1.25 \text{ mm}^{-1}$ ) and those of the skin ( $d = 80 \mu\text{m}$  or  $150 \mu\text{m}$ ) high ( $0.05, 0.5$ – $4 \text{ mm}^{-1}$ ), the inverse algorithm does not give reasonable estimates. In this case, unsatisfactory results of estimating the optical properties of the flesh suggest that the approximation of the homogeneous medium as required by the diffusion model Equation (19) may not be well justified.

Source-detector sensitivity profiles related to a whole apple model covered with a skin layer of thickness  $80 \mu\text{m}$ , are displayed in Figure 8. In order to compute these profiles, the Monte Carlo model requires storing the photons density  $N_{i,j}$  (only contributing to a source-detector pair) in grid elements  $i, j$ , which are related to the cylindrical coordinates  $\rho, z$  ( $\rho = \sqrt{x^2 + y^2}$ ). With this equally spaced system, each volume element is drawn as an annular ring whose radius is  $\rho$ , thickness is  $d\rho$ , and depth is  $dz$ . Let  $N_s$  be the number of photons scored by the detector. Then, the source-detector sensitivity profiles correspond to 2-D plots of the isolines from which the ratio  $\frac{N_{i,j}}{N_s}$  remains fixed and expressed in percent (see color bars). The images (Figure 8) were generated for four source-distance (S-D) equal to 1, 3, 5 and 10 mm (horizontal columns), and different combinations of optical parameter sets ( $\mu_a^{(s)} - \mu'_s^{(s)} = 4 \text{ mm}^{-1}$ ), ( $\mu_a^{(f)} - \mu'_s^{(f)}$ ) corresponding to the vertical columns (a-b-c). First of all, we note that each computed source-detector sensitivity profiles (S-D = 1, 3, 5, and 10 mm) has a well-known banana-shape pattern [55,56] and peaks right beneath the source and detector locations.

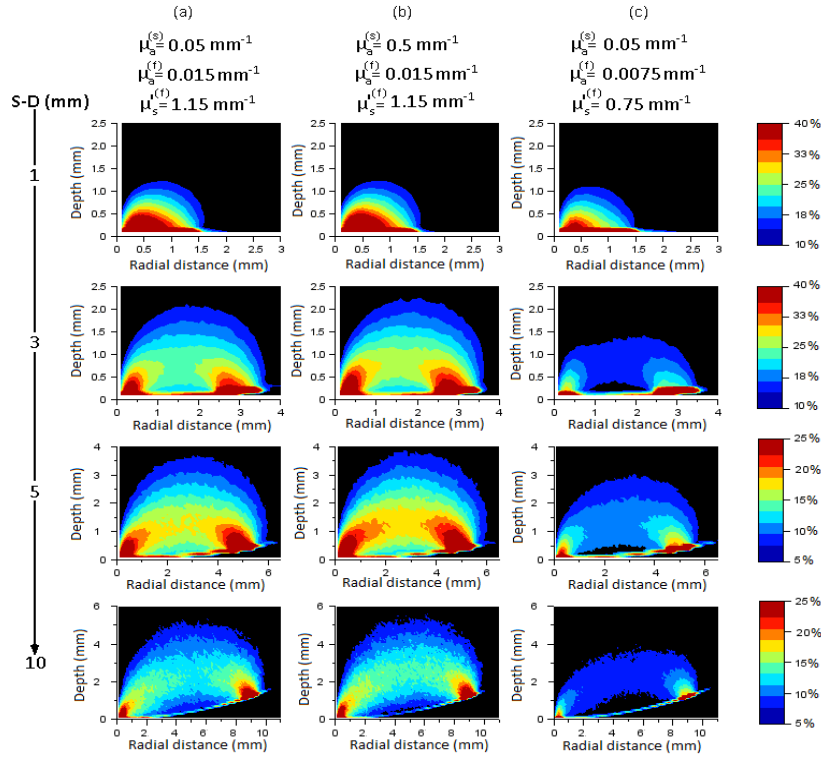


**Figure 8.** Source-detector sensitivity profiles computed for a skin thickness  $d = 80 \mu\text{m}$ , four source-detector distances  $S\text{-}D = 1 \text{ mm}$ ,  $3 \text{ mm}$ ,  $5 \text{ mm}$  and  $10 \text{ mm}$  (horizontal columns), and different combinations of optical properties  $\mu'_s(s) = 4 \text{ mm}^{-1}$ - $\mu_a(s)$ ;  $\mu_a(f)$ - $\mu'_s(f)$  (vertical columns (a-b-c)).

**Table 3.** Retrieved internal optical properties ( $\mu_a$ - $\mu'_s$ ) and errors ( $\Delta\mu_a\%$ ,  $\Delta\mu'_s\%$ ) estimated with respect to the true values ( $\mu_a(f)$ - $\mu'_s(f)$ ).

Input data					Retrieved Data Fit Range (2.8–10 mm)		Relative Error (%)	
d	$\mu_a(s)$	$\mu'_s(s)$	$\mu_a(f)$	$\mu'_s(f)$	$\mu_a$	$\mu'_s$	$\Delta\mu_a$	$\Delta\mu'_s$
0	-	-	0.0075	1.25	0.0076	1.01	1.33%	19.58%
80	0.05	4	0.0075	1.25	0.0111	1.09	48.00%	12.92%
80	0.5	4	0.0075	1.25	0.0125	1.09	66.67%	13.00%
150	0.05	4	0.0075	1.25	0.0102	1.09	36.00%	12.70%
150	0.5	4	0.0075	1.25	0.0124	1.08	65.33%	13.45%
150	0.05	2.5	0.0075	1.25	0.0134	0.71	78.67%	42.92%
0	-	-	0.0225	1.25	0.0203	1.19	9.78%	4.74%
80	0.05	4	0.0225	1.25	0.0233	1.18	3.56%	5.29%
150	0.5	4	0.0225	1.25	0.0264	1.20	17.33%	3.63%
0	-	-	0.0150	1.15	0.0144	1.14	4.00%	0.64%
80	0.05	4	0.0150	1.15	0.0159	1.14	6.00%	0.81%
80	0.5	4	0.0150	1.15	0.0163	1.14	8.67%	0.84%
150	0.05	4	0.0150	1.15	0.0163	1.14	8.87%	0.81%
150	0.5	4	0.0150	1.15	0.0164	1.16	9.93%	0.88%
150	0.05	2.5	0.0150	1.15	0.0173	0.95	15.47%	17.14%
0	-	-	0.0075	0.75	0.0061	0.60	18.67%	19.67%
80	0.05	4	0.0075	0.75	0.0192	0.60	156.00%	19.89%
150	0.5	4	0.0075	0.75	0.0213	0.60	184.00%	19.96%

d: Skin thickness ( $\mu\text{m}$ );  $\mu_a$  ( $\text{mm}^{-1}$ );  $\mu'_s$  ( $\text{mm}^{-1}$ )

The situation is, however, less clear when the detector is close to the source ( $S\text{-}D = 1 \text{ mm}$ ). Nevertheless, photons probe to a depth of about 0.4–0.5 mm, suggesting that reflectance measurements include the contribution of both skin and flesh (subsurface) tissues [57]. As the source-detector distance

is increased (3, 5 and 10 mm), the photons probe more deeply in the flesh, but the depth reached is still dependent on the optical properties of each tissue type (skin, flesh). Therefore, the density of photons is greater in the skin in the case of the column (c) for which  $\mu_a^{(f)} = 0.0075 \text{ mm}^{-1}$ - $\mu_s^{(f)} = 0.75 \text{ mm}^{-1}$  than for the case of the column (a) where  $\mu_a^{(f)} = 0.015 \text{ mm}^{-1}$ - $\mu_s^{(f)} = 1.15 \text{ mm}^{-1}$ . In contrast, there are less photons in the skin in the case of the column (b) ( $\mu_a^{(s)} = 0.5 \text{ mm}^{-1}$ ) than for the case of the column (a) ( $\mu_a^{(s)} = 0.05 \text{ mm}^{-1}$ ).

#### 4. Conclusions

We have proposed novel computational methodologies based on Monte Carlo method to quantitatively study light transport in apple tissues. Monte Carlo simulations were run for apple modeled as a two-layer spherical geometry including the flesh and the skin. Backscattering images and reflectance profiles were simulated for two different spatially-resolved imaging tissue setups, and the resulting reflectance data were analyzed by a semi-infinite photon diffusion model to estimate the optical properties of the flesh.

Learning from various simulation results, we obtained the following conclusions. First of all, even though the skin is considered a thin layer (80  $\mu\text{m}$  or 150  $\mu\text{m}$ ), which is the worst case for applying the diffusion theory to a two-layer tissue model, it is still possible to estimate its effect on optical features with a suitable Monte Carlo approach. Since the Monte Carlo model does not approximate the scattering function, light transport in apple tissue models can be computed with accuracy, even near the light source and skin or flesh boundary.

Both simulated imaging tissue setups (whole apple and half-cut apple models) demonstrate that the internal light dose strongly depends on the presence of the skin. In fact, this thin layer acts like a screen which confines the backscattered photons near the sub-surface of the two-layer spherical model. This will result in a radial reflectance profile that has larger peak intensity compared to the backscattering profile computed with the flesh only. An additional practical issue is the assessment of the internal properties using a spatially homogeneous diffusion model to fit the spatially heterogeneous reflectance data. Because the sensing range is limited from 2.8 mm to 10 mm, the curvature effect of the apple can be ignored in all measurements. However, in this current analysis approach, the relative errors in the estimates are largely dependent on the interplay between the chosen optical parameters for each tissue type. Wrong results are obtained when both the absorption and reduced scattering coefficients of the flesh are low, whereas the best estimates are noted in the case of moderate values. Although the present results can provide useful predictions, additional studies are awaited to assess optical properties of apple samples to compare simulation results with experiments carried out with a steady-state imaging setup.

**Acknowledgments:** This work was funded by the Regional Council of Pays de la Loire and supported by the AI fruit project.

**Author Contributions:** F. Vaudelle developed the Monte Carlo model, M.L. Askoura performed all simulations and J.P. L'Huillier devised the project and wrote the first draft of the manuscript. All authors approved the final manuscript.

**Conflicts of Interest:** The authors declare no conflict of interest.

#### References

1. Cubeddu, R.; D'Andrea, C.; Pifferi, A.; Taroni, P.; Torricelli, A.; Valentini, G.; Dover, C.; Johnson, D.; Ruiz-Altisent, M.; Valero, C. Nondestructive quantification of chemical and physical properties of fruits by time-resolved reflectance spectroscopy in the wavelength range 650–1000 nm. *Appl. Opt.* **2001**, *40*, 538–543. [[CrossRef](#)] [[PubMed](#)]
2. Cubeddu, R.; D'Andrea, C.; Pifferi, A.; Taroni, P.; Torricelli, A.; Valentini, G.; Ruiz-Altisent, M.; Valero, C.; Ortiz, C.; Dover, C. Time-resolved reflectance spectroscopy applied to the nondestructive monitoring of the internal optical properties in apples. *Appl. Spectrosc.* **2001**, *55*, 1368–1374. [[CrossRef](#)]

3. Nicolaï, B.M.; Verlinden, B.E.; Desmet, M.; Saevels, S.; Saeys, W.; Theron, K.; Cubeddu, R.; Pifferi, A.; Torricelli, A. Time-resolved and continuous wave NIR reflectance spectroscopy to predict soluble solids content and firmness of pear. *Postharvest Biol. Technol.* **2008**, *47*, 68–74. [[CrossRef](#)]
4. McGlone, V.; Abe, H.; Kawano, S. Kiwifruit firmness by near infrared light scattering. *J. Near Infrared Spectrosc.* **1997**, *5*, 83–90. [[CrossRef](#)]
5. Il'iasov, S.; Krasnikov, V.V. *Physical Principles of Infrared Irradiation of Foodstuffs*; Hemisphere Pub. Corp.: Summit, NJ, USA, 1991.
6. Watté, R.; Aernouts, B.; Van Beers, R.; Herremans, E.; Ho, Q.T.; Verboven, P.; Nicolaï, B.; Saeys, W. Modeling the propagation of light in realistic tissue structures with mmc-fpf: A meshed monte carlo method with free phase function. *Opt. Express* **2015**, *23*, 17467–17486. [[CrossRef](#)] [[PubMed](#)]
7. Tuchin, V.V.; Maksimova, I.L.; Zimnyakov, D.A.; Kon, I.L.; Mavlyutov, A.H.; Mishin, A.A. Light propagation in tissues with controlled optical properties. *J. Biomed. Opt.* **1997**, *2*, 401–417. [[CrossRef](#)] [[PubMed](#)]
8. Cheong, W.-F.; Prahl, S.A.; Welch, A.J. A review of the optical properties of biological tissues. *IEEE J. Quantum Electron.* **1990**, *26*, 2166–2185. [[CrossRef](#)]
9. Welch, A.J.; Van Gemert, M.J. *Optical-Thermal Response of Laser-Irradiated Tissue*; Springer: New York, NY, USA, 1995; Vol. 1.
10. Gibson, A.; Hebden, J.; Arridge, S.R. Recent advances in diffuse optical imaging. *Phys. Med. Biol.* **2005**, *50*. [[CrossRef](#)]
11. Kienle, A.; Patterson, M.S. Improved solutions of the steady-state and the time-resolved diffusion equations for reflectance from a semi-infinite turbid medium. *J. Opt. Soc. Am. A* **1997**, *14*, 246–254. [[CrossRef](#)]
12. Farrell, T.J.; Patterson, M.S.; Wilson, B. A diffusion theory model of spatially resolved, steady-state diffuse reflectance for the noninvasive determination of tissue optical properties *in vivo*. *Med. Phys.* **1992**, *19*, 879–888. [[CrossRef](#)] [[PubMed](#)]
13. Contini, D.; Martelli, F.; Zaccanti, G. Photon migration through a turbid slab described by a model based on diffusion approximation. I. Theory. *Appl. Opt.* **1997**, *36*, 4587–4599. [[CrossRef](#)] [[PubMed](#)]
14. Qin, J.; Lu, R. Hyperspectral diffuse reflectance imaging for rapid, noncontact measurement of the optical properties of turbid materials. *Appl. Opt.* **2006**, *45*, 8366–8373. [[CrossRef](#)] [[PubMed](#)]
15. Peng, Y.; Lu, R. Analysis of spatially resolved hyperspectral scattering images for assessing apple fruit firmness and soluble solids content. *Postharvest Biol. Technol.* **2008**, *48*, 52–62. [[CrossRef](#)]
16. Cen, H.; Lu, R.; Mendoza, F.; Beaudry, R.M. Relationship of the optical absorption and scattering properties with mechanical and structural properties of apple tissue. *Postharvest Biol. Technol.* **2013**, *85*, 30–38. [[CrossRef](#)]
17. Lorente, D.; Zude, M.; Idler, C.; Gómez-Sanchis, J.; Blasco, J. Laser-light backscattering imaging for early decay detection in citrus fruit using both a statistical and a physical model. *J. Food Eng.* **2015**, *154*, 76–85. [[CrossRef](#)]
18. Valero, C.; Ruiz-Altisent, M.; Cubeddu, R.; Pifferi, A.; Taroni, P.; Torricelli, A.; Valentini, G.; Johnson, D.; Dover, C. Selection models for the internal quality of fruit, based on time domain laser reflectance spectroscopy. *Biosyst. Eng.* **2004**, *88*, 313–323. [[CrossRef](#)]
19. Chauchard, F.; Roger, J.; Bellon-Maurel, V.; Abrahamsson, C.; Andersson-Engels, S.; Svanberg, S. Madstress: A linear approach for evaluating scattering and absorption coefficients of samples measured using time-resolved spectroscopy in reflection. *Appl. Spectrosc.* **2005**, *59*, 1229–1235. [[CrossRef](#)] [[PubMed](#)]
20. Vaudelle, F.; L'Huillier, J.-P. Influence of the size and skin thickness of apple varieties on the retrieval of internal optical properties using VIS/NIR spectroscopy: A monte carlo-based study. *Comput. Electron. Agric.* **2015**, *116*, 137–149. [[CrossRef](#)]
21. Schmitt, J.; Wall, R.; Zhou, G.; Walker, E. Multilayer model of photon diffusion in skin. *JOSA A* **1990**, *7*, 2141–2153. [[CrossRef](#)]
22. Kienle, A.; Patterson, M.S.; Dögnitz, N.; Bays, R.; Wagnieres, G.; van Den Bergh, H. Noninvasive determination of the optical properties of two-layered turbid media. *Appl. Opt.* **1998**, *37*, 779–791. [[CrossRef](#)] [[PubMed](#)]
23. Cen, H.; Lu, R. Quantification of the optical properties of two-layer turbid materials using a hyperspectral imaging-based spatially-resolved technique. *Appl. Opt.* **2009**, *48*, 5612–5623. [[CrossRef](#)] [[PubMed](#)]
24. Arridge, S.; Schweiger, M.; Hiraoka, M.; Delpy, D. A finite element approach for modeling photon transport in tissue. *Med. Phys.* **1993**, *20*, 299–309. [[CrossRef](#)] [[PubMed](#)]



25. Aydin, E.; Katsimichas, S.; de Oliveira, C. Time-dependent diffusion and transport calculations using a finite-element-spherical harmonics method. *J. Quant. Spectrosc. Radiat. Transf.* **2005**, *95*, 349–363. [[CrossRef](#)]
26. Deulin, X.; L'Huillier, J.P. Finite element approach to photon propagation modeling in semi-infinite homogeneous and multilayered tissue structures. *Eur. Phys. J. Appl. Phys.* **2006**, *33*, 133–146. [[CrossRef](#)]
27. Wang, L.; Jacques, S.L.; Zheng, L. MCML-Monte Carlo modeling of light transport in multi-layered tissues. *Comput. Methods Prog. Biomed.* **1995**, *47*, 131–146. [[CrossRef](#)]
28. Okada, K. Extended time dependent dielectric breakdown model based on anomalous gate area dependence of lifetime in ultra thin silicon dioxides. *Jpn. J. Appl. Phys.* **1997**, *36*, 1443–1447. [[CrossRef](#)]
29. Mansouri, C.; L'Huillier, J.-P.; Kashou, N.H.; Humeau, A. Depth sensitivity analysis of functional near-infrared spectroscopy measurement using three-dimensional monte carlo modelling-based magnetic resonance imaging. *Lasers Med. Sci.* **2010**, *25*, 431–438. [[CrossRef](#)] [[PubMed](#)]
30. Vaudelle, F.; L'huillier, J.-P. Time-resolved optical fluorescence spectroscopy of heterogeneous turbid media with special emphasis on brain tissue structures including diseased regions: A sensitivity analysis. *Opt. Commun.* **2013**, *304*, 161–168. [[CrossRef](#)]
31. Eze, R.; Kumar, S. Laser transport through thin scattering layers. *Appl. Opt.* **2010**, *49*, 358–368. [[CrossRef](#)] [[PubMed](#)]
32. Zamora-Rojas, E.; Garrido-Varo, A.; Aernouts, B.; Pérez-Marín, D.; Saeys, W.; Yamada, Y.; Guerrero-Ginel, J.E. Understanding near infrared radiation propagation in pig skin reflectance measurements. *Innov. Food Sci. Emerg. Technol.* **2014**, *22*, 137–146. [[CrossRef](#)]
33. Meglinski, I.V.; Matcher, S.J. Quantitative assessment of skin layers absorption and skin reflectance spectra simulation in the visible and near-infrared spectral regions. *Physiol. Meas.* **2002**, *23*, 741–753. [[CrossRef](#)] [[PubMed](#)]
34. Boas, D.; Culver, J.; Stott, J.; Dunn, A. Three dimensional monte carlo code for photon migration through complex heterogeneous media including the adult human head. *Opt. Express* **2002**, *10*, 159–170. [[CrossRef](#)] [[PubMed](#)]
35. Qin, J.; Lu, R. Monte carlo simulation for quantification of light transport features in apples. *Comput. Electron. Agric.* **2009**, *68*, 44–51. [[CrossRef](#)]
36. Baranyai, L.; Zude, M. Analysis of laser light propagation in kiwifruit using backscattering imaging and monte carlo simulation. *Comput. Electron. Agric.* **2009**, *69*, 33–39. [[CrossRef](#)]
37. Wang, W.; Li, C. Measurement of the light absorption and scattering properties of onion skin and flesh at 633 nm. *Postharvest Biol. Technol.* **2013**, *86*, 494–501. [[CrossRef](#)]
38. Ishimaru, A. *Wave Propagation and Scattering In Random Media. Volume I-Single Scattering And Transport Theory*; New York Academic Press Inc.: New York, NY, USA, 1978; p. 267.
39. Askoura, M.L.; Piron, V.; Vaudelle, F.; L'Huillier, J.-P.; Madieta, E.; Mehinagic, E. Experimental investigation on light propagation through apple tissue structures. *Proc. SPIE* **2015**, 9542. [[CrossRef](#)]
40. Peng, Y.; Lu, R. Improving apple fruit firmness predictions by effective correction of multispectral scattering images. *Postharvest Biol. Technol.* **2006**, *41*, 266–274. [[CrossRef](#)]
41. Zhang, F.; Kinnunen, M.; Popov, A.; Myllylä, R. Monte carlo method for simulating optical coherence tomography signal in homogeneous turbid media. *Proc. SPIE* **2007**, 7022. [[CrossRef](#)]
42. Prahl, S.A.; Keijzer, M.; Jacques, S.L.; Welch, A.J. A monte carlo model of light propagation in tissue. *Dosim. Laser Radiat. Med. Biol.* **1989**, *5*, 102–111.
43. Prahl, S.A.; van Gemert, M.J.; Welch, A.J. Determining the optical properties of turbid media by using the adding-doubling method. *Appl. Opt.* **1993**, *32*, 559–568. [[CrossRef](#)] [[PubMed](#)]
44. Witt, A.N. Multiple scattering in reflection nebulae. Ii. Uniform plane-parallel nebulae with foreground stars. *Astrophys. J. Suppl. Ser.* **1977**, *35*, 7–19. [[CrossRef](#)]
45. Castro, D.C.; Álvarez, N.; Gabriel, P.; Micheloud, N.; Buyatti, M.; Gariglio, N. Crop loading studies on “caricia” and “eva” apples grown in a mild winter area. *Sci. Agric.* **2015**, *72*, 237–244. [[CrossRef](#)]
46. Konarska, A. The structure of the fruit peel in two varieties of malus domestica borkh.(rosaceae) before and after storage. *Protoplasma* **2013**, *250*, 701–714. [[CrossRef](#)] [[PubMed](#)]
47. Homutova, I.; Blažek, J. Differences in fruit skin thickness between selected apple (malus domestica borkh.) cultivars assessed by histological and sensory methods. *Hortic. Sci.* **2006**, *33*, 108–113.



48. Rowe, P.I.; Künnemeyer, R.; McGlone, A.; Talele, S.; Martinsen, P.; Seelye, R. Relationship between tissue firmness and optical properties of “royal gala” apples from 400 to 1050 nm. *Postharvest Biol. Technol.* **2014**, *94*, 89–96. [[CrossRef](#)]
49. Lu, R.; Cen, H.; Huang, M.; Ariana, D.P. Spectral absorption and scattering properties of normal and bruised apple tissue. *Trans. ASABE* **2010**, *53*, 263–269. [[CrossRef](#)]
50. Saeys, W.; Velazco-Roa, M.A.; Thennadil, S.N.; Ramon, H.; Nicolai, B.M. Optical properties of apple skin and flesh in the wavelength range from 350 to 2200 nm. *Appl. Opt.* **2008**, *47*, 908–919. [[CrossRef](#)] [[PubMed](#)]
51. Keijzer, M.; Jacques, S.L.; Prahl, S.A.; Welch, A.J. Light distributions in artery tissue: Monte carlo simulations for finite-diameter laser beams. *Lasers Surg. Med.* **1989**, *9*, 148–154. [[CrossRef](#)] [[PubMed](#)]
52. Kienle, A.; Lilge, L.; Patterson, M.S.; Hibst, R.; Steiner, R.; Wilson, B.C. Spatially resolved absolute diffuse reflectance measurements for noninvasive determination of the optical scattering and absorption coefficients of biological tissue. *Appl. Opt.* **1996**, *35*, 2304–2314. [[CrossRef](#)] [[PubMed](#)]
53. Haskell, R.C.; Svaasand, L.O.; Tsay, T.-T.; Feng, T.-C.; McAdams, M.S.; Tromberg, B.J. Boundary conditions for the diffusion equation in radiative transfer. *J. Opt. Soc. Am. A* **1994**, *11*, 2727–2741. [[CrossRef](#)]
54. Qin, J.; Lu, R. Measurement of the optical properties of fruits and vegetables using spatially resolved hyperspectral diffuse reflectance imaging technique. *Postharvest Biol. Technol.* **2008**, *49*, 355–365. [[CrossRef](#)]
55. Lee, K. Optical mammography: Diffuse optical imaging of breast cancer. *World J. Clin. Oncol.* **2011**, *2*, 64–72. [[CrossRef](#)] [[PubMed](#)]
56. Feng, S.; Zeng, F.-A.; Chance, B. Photon migration in the presence of a single defect: A perturbation analysis. *Appl. Opt.* **1995**, *34*, 3826–3837. [[CrossRef](#)] [[PubMed](#)]
57. Do Trong, N.N.; Rizzolo, A.; Herremans, E.; Vanoli, M.; Cortellino, G.; Erkinbaev, C.; Tsuta, M.; Spinelli, L.; Contini, D.; Torricelli, A. Optical properties-microstructure-texture relationships of dried apple slices: Spatially resolved diffuse reflectance spectroscopy as a novel technique for analysis and process control. *Innov. Food Sci. Emerg. Technol.* **2014**, *21*, 160–168. [[CrossRef](#)]



© 2015 by the authors; licensee MDPI, Basel, Switzerland. This article is an open access article distributed under the terms and conditions of the Creative Commons by Attribution (CC-BY) license (<http://creativecommons.org/licenses/by/4.0/>).